
Article:
Guan, D., Gao, J., Sharp, J. et al. (2018) Enhancing ductility and strength of nanostructured Mg alloy by in-situ powder casting during spark plasma sintering. Journal of Alloys and Compounds, 769. pp. 71-77. ISSN: 0925-8388

https://doi.org/10.1016/j.jallcom.2018.07.247

Enhancing Ductility and Strength of Nanostructured Mg Alloy by *in-situ* Powder Casting during Spark Plasma Sintering

Dikai Guan*, Junheng Gao, Joanne Sharp, W. Mark Rainforth*

Department of Materials Science and Engineering, University of Sheffield, Sheffield, S1 3JD, UK

*Corresponding authors: dikai.guan@sheffield.ac.uk, m.rainforth@sheffield.ac.uk

Abstract： Due to internal processing defects, bulk nanostructured Mg alloys have high strength but extremely poor ductility. A novel and facile process was designed and *in-situ* powder casting was initiated during spark plasma sintering. This process significantly reduced processing induced defects, enhanced inter-particle bonding and introduced significant precipitation without extra ageing treatment, leading to improvement of the compressive strength and ductility. The compressive strain of bulk sample consisting of pure cryomilled powder was 3.6% with an ultimate strength of 500 MPa, while cryomilled powder mixed with eutectic Mg-Zn alloy powder obtained a compressive strain of 6.6% and ultimate strength of 506 MPa. The ductility of the sample with mixed powder was increased by 83% without any sacrifice of strength compared to the sample consisting of only pure cryomilled powder.

Keywords: Nanostructure materials; Magnesium; Ductility; Spark plasma sintering

1. Introduction

Strength and ductility are often used as the two most important parameters to evaluate mechanical properties of metals and alloys. However, an increase in strength and ductility are generally mutual exclusive in bulk nanostructured (NS) metals and alloys[1-6]. Bulk NS metals and alloys, with structural features less than 100 nm in at least one dimension can be obtained by either a "one-step" method such as severe plastic deformation[7-9], or a "two-step" approach such as powder consolidation[10, 11]. The former strategy can produce defect-free bulk NS material with higher ductility than those fabricated by the latter approach. However, even these NS materials with exceptionally high strength usually exhibit poor ductility[4]. Recently, several strategies have been reported to enhance the ductility of bulk ultra-fine grained and NS materials[12]. Introducing a bimodal or multi-grain size distribution[2, 13], pre-existing nanoscale twins[14, 15], and engineering nanoscale precipitates into the matrix by ageing [5, 16, 17] have been widely studied. Nevertheless, most of these strategies either sacrifice some of strength or are only used in a "one-step" approach. The largest problem for bulk NS metals and alloys produced by a "two-step" approach is those materials often have artefacts such as porosity and incomplete inter-particle bonding, which results in very low ductility (<5% elongation to failure)[4].

It is extremely difficult to obtain fully dense samples with complete inter-particle bonding in these nanocrystalline (NC) powders[18]. To soften NC particles, high processing temperatures have to be employed, to promote plastic deformation to allow better filling and higher diffusion rates[18]. However, high temperature also leads to grain coarsening and therefore the loss of the NC structure[18, 19]. Koch and co-workers designed a novel approach and produced fully dense bulk NS Cu spheres via *in-situ* consolidation which involved the combination of liquid nitrogen and room temperature milling [20]. Liu et al. [21]

produced high-strength Mo alloys with unprecedented ductility using a molecular-level liquid–liquid mixing/doping technique.

Most of the strategies noted above have been applied to bulk NS Cu[20], Ni[13], Al[5, 16], Ti [22, 23] and their alloys, but rarely to Mg or its alloys. Bulk NS Mg alloys present particular challenges associated with the low ductility due to limited slip systems[24], suppressed twining in NC grains[25, 26] and its inherent high reactivity. In contrast, Mg alloys are very attractive given their low density, and high specific stiffness and strength[27]. Kawamura et al. reported a Mg97Zn1Y2 alloy produced by rapidly solidified powder metallurgy and subsequent hot extrusion. This sample had a high tensile strength of 610 MPa, but with limited elongation of 5% at room temperature[6]. Recently, bulk NS AZ80 and Mg-10Al alloys have been fabricated by a combination of cryomilling and spark plasma sintering (SPS) [28, 29]. Both alloys exhibited an exceptionally high compressive strength, but with the usual poor ductility (average compressive strains were only 3.7% and 2.3%). The low ductility has been attributed to the internal defects and insufficient inter-particle bonding after sintering[28]. Clearly, the challenge is to find a processing method that produces both high strength and high ductility.

In this paper, we firstly designed a novel process where *in-situ* powder casting was initiated during SPS by introducing a very low melting temperature eutectic Mg-Zn alloy powder into nanostructured Mg particles. Fig. 1 gives schematics showing the microstructural evolution expected during *in-situ* powder casting when the sample was consolidated by SPS. During heating, the Mg-Zn particles melted and flowed along NC Mg particles boundaries, filling the internal defects. At the same time, Zn atoms partly dissolved into the solid Mg matrix by diffusion resulting in the formation of precipitates from the oversaturated Mg matrix during subsequent cooling. This process can simultaneously significantly remove internal pores, enhance the inter-particle bounding between nanostructured Mg particles and

introduce very small dense precipitates into bulk NS Mg alloy with no time-consuming ageing treatment. Consequently, the ductility of bulk NS Mg alloy was improved without loss of strength.

2. Experimental

9.7 g pure Mg (99.99%) and 10.3 g zinc (99.99%) ingots were used to produce a eutectic alloy with a composition of Mg48.7Zn51.3 (wt. %) by using small scale melting. After casting, this brittle eutectic ingot was cryomilled for 5 minutes to obtain fine particles. The melting temperature of the eutectic alloy powder was measured using DTA. The sample was heated from room temperature to 400 °C in argon with rate of 10 °C/min.

A sample designated as CM6h was cryomilled for 6h and consolidated by SPS. The sample preparation procedure can be found in our previous study [30]. A mixture of 80 wt.% cryomilled powder and 20 wt.% Mg-Zn eutectic alloy (EA) powder was fully mixed by cryomilling without grinding balls and consolidated into bulk samples under the same conditions (designated as CM6h+EA sample). For comparison purposes, as-received AZ31 powder was consolidated to form coarse grain sized sample (designated as CG sample).

Cubic compression specimens (4×4×4 mm^3) were polished before compression testing. The tests were conducted using Zwick/Roell universal testing machine at a crosshead speed of 0.06 mm/min until failure. At least 3 specimens were tested for each sample. The loading direction for testing was normal to the disk-shaped sample surface. All experimental data have been corrected for machine compliance[31].

Sample preparation for XRD and SEM experiments were illustrated in [30]. Thin foils TEM specimens were initially mechanically ground to 25 μm and finally thinned by ion milling with an Ar^+ accelerating voltage of 3 kV and liquid nitrogen cooling system. An FEI Tecnai 20, operating at 200 kV, was used for TEM characterization.

3. Results and discussion

Fig. 2 shows a DTA curve of eutectic alloy powder. An endothermic peak clearly indicated the melting temperature of this powder was around 349.1 °C. Fig. 3 shows the XRD pattern of eutectic alloy powder. The main phase in this powder is $Mg_{51.04}Zn_{19.8}$ (at. %) as expected. Fig. 4(a) shows the morphology of the eutectic powder. The average particle size after 5 minutes cryomilling was approximately 20 μm (Fig. 4(b)). Fig. 4(c-d) present elemental analyses collected from particles A and B by EDS. The results show the composition from the particles was very close to the original designing composition of $Mg_{48.7}Zn_{51.3}$ (wt. %), which agreed well with the results of XRD (Fig. 3).

Fig. 5 shows the variation of sintering temperature, piston force, and piston speed as functions of running time from samples CM6h and CM6h+EA. Compared with sample CM6h, a visible rapid piston movement peak appeared when sintering temperature was up to 330-350 °C in sample CM6h+EA only. The appearance of this extra peak can be attributed to the melting of eutectic alloy powder during sintering.

Fig. 6(a) shows the true compressive stress-strain curves of CM6h, CM6h+EA, as well as reference CG samples. The corresponding compressive properties are listed in Table 1. 0.2% yield compressive strength of CG, CM6h and CM6h+EA samples were 187 MPa, 400 MPa and 408 MPa, respectively. The corresponding ultimate compressive strengths were 363 MPa, 500 MPa and 506 MPa, respectively. Both yield and ultimate strength of CM6h+EA are slightly greater than that of CM6h sample. For compressive strains at the ultimate compressive strength, the CM6h sample had a low strain of 3.6%. Conversely, after adding the Mg-Zn eutectic alloy, the compressive strain of sample CM6h+EA increased to 6.6%, which improved the ductility of bulk NS sample by 83% without any sacrifice of strength.

Fig. 6(b) summarizes the ultimate compressive strength versus strain. The compression test data were collected from published papers and this study related to bulk NS

Mg alloys produced by "two-step" approaches [28, 29, 32, 33]. Most of the published results, and the present results from the CM6h samples, are positioned to the left hand side of trend line, showing an inverse relationship between the strength and ductility. However, the results from CM6h+EA samples stand out from the trend, exhibiting an unusually good combination of high strength with enhanced ductility in the field of bulk NS Mg alloys.

Fig. 7 shows typical backscattered electron SEM images of samples CM6h and CM6h+EA. Considerable porosity was observed in CM6h sample (Fig. 7(a)), arising from either incomplete consolidation or particle pull-out during polishing because of insufficient inter-particle bonding. However, these pores were largely absent in sample CM6h+EA (Fig. 7(b)). The reason can be found in Fig. 5. A rapid piston movement occurred around 350 °C for the CM6h+EA only, which corresponds to the point at which the Mg-Zn eutectic alloy powder melted. From the microstructural evidence, the liquid phase flowed between solid NC Mg particles and filled potential voids or gaps during consolidation by SPS, forming a fully dense sample during cooling.

Fig. 8(a) shows representative bright-field TEM micrographs and selected area electron diffraction (SAED) pattern of the bulk NS CM6h sample. Fig. 8(b) gives the grain size distribution of the largely equiaxed grains, which varied in the range from 10 to 80 nm, with an average grain size of 37 nm (>200 measured grains). The grain size of the sintered sample was bigger than the corresponding cryomilled powder (26.2±7.9 nm[30]) due to grain growth during the SPS process. Coarse grains were also observed among the NC grains. The formation of these coarse grains was probably due to the absence of pinning particles, allowing rapid grain growth, but may have also been due to localized higher temperature and stress at points of contact area between initially separate particles during SPS process[28, 34, 35]. A typical bright-field TEM image and SAED pattern of the bulk NS CM6h+EA sample are presented in Fig. 8(c). The grain size and morphology were similar to the bulk NS CM6h

sample (Fig. 8(b)). However, a high density of fine precipitates can be observed in CM6h+EA sample. Fig. 9 gives TEM images from coarse and fine grain areas in sample CM6h+EA. Precipitates were clearly observed in both coarse and NC grains. Precipitate sequence in Mg-Zn alloy system has been widely investigated in the past and documented as "supersaturated solid solution→ G.P. zones→ β_1'→ β_2'→ β"[36-39]. The metastable phases in this sample could either be β_1' or β_2' phase or both. β_1' was reported to have a hexagonal structure similar to $MgZn_2$ and recently reported to have a base-centred monoclinic structure similar to Mg_4Zn_7[38, 39]. β_1' with the base-centred monoclinic structure is quite different from β_2' with a hexagonal structure similar to $MgZn_2$. Therefore, only one set of SAED patterns was used in this work to identify the precipitate type by matching the reported SAED patterns in the literature[36-39].

According to SAED pattern and recognised publications[36-39], most of these precipitates in large grains (Fig. 9(a)) can be indexed as β_1' strengthening phases with the base-centered monoclinic structure (a = 2.596 nm, b = 1.428 nm, c = 0.524 nm, γ = 102.5°) and an orientation relationship with matrix was $[0\ 0\ 1]_{\beta_1'}//[0\ 0\ 0\ 1]_\alpha$ and $(6\ 3\ 0)_{\beta_1'}//(0\ 1\ \bar{1}\ 0)_\alpha$. In addition, different shapes and orientations of precipitates can be observed in the same fine grain in Fig. 9(b). This could be attributed to several reasons. Firstly, β_1' and β_2' co-existed in the same fine grain area and certainly these two phases have different orientations with matrix. Secondly, both β_1' and β_2' were reported to have different orientations with Mg matrix. For example, Gao et al. reported the blocky type precipitates were also indexed as β_1' phase but with a different orientation relationship with the matrix ($[0\ 0\ 1]_{\beta_1'}//[1\ 0\ \bar{1}\ 0]_\alpha$ and $(2\ 5\ 0)_{\beta_1'}//(0\ 0\ 0\ 1)_\alpha$)[39]. Most recently, Jiang et al. found new orientations between precipitate β_2' and matrix ($([\bar{2}\ 1\ 1\ 0]_{\beta_2'}//[0\ 1\ \bar{1}\ 0]_\alpha$ and $(0\ 1\ \bar{1}\ 5)_{\beta_2'}//(\bar{2}\ 1\ 1\ 0)_\alpha$)[36]. This indicates, as well as forming a liquid phase during SPS processing, the Zn also diffused and dissolved into

surrounding solid Mg particles. As the solubility for Zn in Mg fell during cooling, a high density of fine strengthening precipitates was produced (Fig. 1 and Figs. 7-9).

The only difference in the whole process between samples CM6h and CM6h+EA was 20% (wt.%) cryomilled powder was replaced by Mg-Zn eutectic alloy powder. Therefore, the improvement of mechanical properties of sample CM6h+EA can be contributed to the additions of Mg-Zn eutectic alloy powder.

Comparing mechanical properties in Table 1, adding Mg-Zn eutectic alloy powder slightly increased the strength of sample CM6h+EA. Considering all the differences between samples CM6h and CM6h+EA, the mechanisms contributing to the improved strength of sample CM6h+EA are as follows: more compact microstructure, solid solution strengthening and precipitate strengthening.

Processing artefacts such as internal pores are very common in bulk NS materials produced by "two-step" approach. It causes early failure even before reaching the yielding point in some conditions. Even though when the theoretical density is obtained in some cases, the inter-particle bonding is not sufficient. In this study, residual Mg-Zn phase that did not dissolve in the NC Mg particles solidified in between the solid Mg particles, removing the residual porosity and improved the inter-particle bonding of CM6h+EA sample (Fig. 7(b)).

During sintering above the melting temperature of Mg-Zn eutectic alloy, liquid Zn atoms diffused into the Mg matrix with a relative high diffusion rate. During the cooling stage, some of the Zn atoms still stayed in Mg as solid solutions, while the other came out from Mg matrix in the form of precipitates. Extra solute Zn atoms introduced by *in-situ* powder casting impose lattice strains on adjacent Mg atoms. The lattice strain field can hinder the movement of dislocations and increase the strength. In addition, a high density of strengthening precipitates including β_1' and β_2' were observed only in sample CM6h+EA,

which resulted from the *in-situ* powder casting. These fine precipitate can act as barriers to impede the movement of dislocations and therefore increased the strength.

As mentioned earlier, high strength and poor ductility is the common feature of bulk NS materials[1-3, 5, 40]. It is recognized that low ductility of bulk NS materials is caused by either extrinsic defects such as porosity, insufficient inter-particle bonding or intrinsic effects such as low strain hardening/dislocation storage capacity[5, 15]. In the current study, the *in-situ* powder casting during SPS has largely reduced the internal defects and enhanced the poor inter-particle bonding associated (Fig. 7). Furthermore, a large amount of nano-sized precipitates appeared in both coarse and NC grains with no ageing process (Figs. 8-9). The improved compressive strain without sacrificing strength in the CM6h+EA sample can be attributed to the significant reduction in processing defects as well as the precipitation hardening. In addition, compared to the true stress-strain curves of bulk CM6h sample (Fig. 6(a)), much greater compressive strain was observed in CM6h+EA sample. This was most probably a result of two factors. Firstly, the presence of defects and incomplete inter-particle bonding in the CM6h sample would have limited the ductility. Secondly, the precipitation in CM6h+EA would have promoted greater strain hardening due to increased interaction with dislocations in grain interiors.

4. Conclusions

In summary, we have firstly demonstrated a facile strategy to enhance ductility without the sacrifice of strength in a bulk nanostructured Mg alloy via *in-situ* powder casting during SPS. This process significantly reduced processing induced defects, enhanced inter-particle bonding and introduced significant precipitation without extra ageing treatment. Overall, sample CM6h+EA obtained a best combination of ductility (6.6%) and ultimate strength (506 MPa) among all samples, which produced better ductility than those of previously reported research related to bulk NS Mg alloys [28, 29, 32, 33]. This strategy can

be also extended to other alloy systems (e.g., Ti-Al or Al-Zn-Mg) which possess intermetallic with low melting temperatures. The cryomilling and SPS used in this study could be easily modified to current industrial process or extended to other consolidation techniques, and has the potential for large-scale application of producing bulk dense NS materials by "two-step" approaches.

Acknowledgements

This work was funded by the EPSRC (EP/L025213/1), the University of Sheffield and China Scholarship Council.

Declarations of interest: none

References

[1] Y.T. Zhu, X. Liao, Nanostructured metals: Retaining ductility, Nat. Mater. 3 (2004) 351-352.
[2] Y. Wang, M. Chen, F. Zhou, E. Ma, High tensile ductility in a nanostructured metal, Nature 419 (2002) 912-915.
[3] X. Huang, N. Hansen, N. Tsuji, Hardening by Annealing and Softening by Deformation in Nanostructured Metals, Science 312 (2006) 249-251.
[4] C. Koch, Optimization of strength and ductility in nanocrystalline and ultrafine grained metals, Scr. Mater. 49 (2003) 657-662.
[5] Y.H. Zhao, X.Z. Liao, S. Cheng, E. Ma, Y.T. Zhu, Simultaneously Increasing the Ductility and Strength of Nanostructured Alloys, Adv. Mater. 18 (2006) 2280-2283.
[6] Y. Kawamura, K. Hayashi, A. Inoue, T. Masumoto, Rapidly Solidified Powder Metallurgy Mg97Zn1Y2 Alloys with Excellent Tensile Yield Strength above 600 MPa, Mater. Trans. 42 (2001) 1172-1176.
[7] R. Valiev, Nanostructuring of metals by severe plastic deformation for advanced properties, Nat. Mater. 3 (2004) 511-516.
[8] L. Tang, Y. Zhao, R.K. Islamgaliev, R.Z. Valiev, Y.T. Zhu, Microstructure and thermal stability of nanocrystalline Mg-Gd-Y-Zr alloy processed by high pressure torsion, J. Alloys Compd. 721 (2017) 577-585.
[9] H. Gleiter, Nanostructured materials: basic concepts and microstructure, Acta Mater. 48 (2000) 1-29.
[10] D.B. Witkin, E.J. Lavernia, Synthesis and mechanical behavior of nanostructured materials via cryomilling, Prog. Mater Sci. 51 (2006) 1-60.
[11] M. Pozuelo, C. Melnyk, W.H. Kao, J.-M. Yang, Cryomilling and spark plasma sintering of nanocrystalline magnesium-based alloy, J. Mater. Res. 26 (2011) 904-911.
[12] Y. Zhao, Y. Zhu, E.J. Lavernia, Strategies for Improving Tensile Ductility of Bulk Nanostructured Materials, Adv. Eng. Mater. 12 (2010) 769-778.
[13] Y. Zhao, T. Topping, J.F. Bingert, J.J. Thornton, A.M. Dangelewicz, Y. Li, W. Liu, Y. Zhu, Y. Zhou, E.J. Lavernia, High Tensile Ductility and Strength in Bulk Nanostructured Nickel, Adv. Mater. 20 (2008) 3028-3033.
[14] L. Lu, Y. Shen, X. Chen, L. Qian, K. Lu, Ultrahigh Strength and High Electrical Conductivity in Copper, Science 304 (2004) 422-426.
[15] Y.H. Zhao, J.F. Bingert, X.Z. Liao, B.Z. Cui, K. Han, A.V. Sergueeva, A.K. Mukherjee, R.Z. Valiev, T.G. Langdon, Y.T. Zhu, Simultaneously Increasing the Ductility and Strength of Ultra-Fine-Grained Pure Copper, Adv. Mater. 18 (2006) 2949-2953.

[16] Z. Horita, K. Ohashi, T. Fujita, K. Kaneko, T.G. Langdon, Achieving High Strength and High Ductility in Precipitation-Hardened Alloys, Adv. Mater. 17 (2005) 1599-1602.
[17] A.R. Kalidindi, C.A. Schuh, Stability criteria for nanocrystalline alloys, Acta Mater. 132 (2017) 128-137.
[18] C.C. Koch, Synthesis of nanostructured materials by mechanical milling: problems and opportunities, Nanostruct. Mater. 9 (1997) 13-22.
[19] P.G. Sanders, G.E. Fougere, L.J. Thompson, J.A. Eastman, J.R. Weertman, IMPROVEMENTS IN THE SYNTHESIS AND COMPACTION OF NANOCRYSTALLINE MATERIALS, Nanostruct. Mater. 8 (1997) 243-252.
[20] K.M. Youssef, R.O. Scattergood, K.L. Murty, J.A. Horton, C.C. Koch, Ultrahigh strength and high ductility of bulk nanocrystalline copper, Appl. Phys. Lett. 87 (2005) 091904-091903.
[21] G. Liu, G.J. Zhang, F. Jiang, X.D. Ding, Y.J. Sun, J. Sun, E. Ma, Nanostructured high-strength molybdenum alloys with unprecedented tensile ductility, Nat. Mater. 12 (2013) 344-350.
[22] O. Ertorer, T. Topping, Y. Li, W. Moss, E.J. Lavernia, Enhanced tensile strength and high ductility in cryomilled commercially pure titanium, Scr. Mater. 60 (2009) 586-589.
[23] R. Valiev, The effect of annealing on tensile deformation behavior of nanostructured SPD titanium, Scr. Mater. 49 (2003) 669-674.
[24] H.E. Friedrich, B.L. Mordike, Magnesium Technology: Metallurgy, Design Data, Applications, Springer, New York, 2010.
[25] X.L. Wu, K.M. Youssef, C.C. Koch, S.N. Mathaudhu, L.J. Kecskés, Y.T. Zhu, Deformation twinning in a nanocrystalline hcp Mg alloy, Scr. Mater. 64 (2011) 213-216.
[26] Y. Zhu, X. Liao, X. Wu, Deformation twinning in bulk nanocrystalline metals: Experimental observations, JOM 60 (2008) 60-64.
[27] S.R. Agnew, J.F. Nie, Preface to the viewpoint set on: The current state of magnesium alloy science and technology, Scr. Mater. 63 (2010) 671-673.
[28] B. Zheng, O. Ertorer, Y. Li, Y. Zhou, S.N. Mathaudhu, C.Y.A. Tsao, E.J. Lavernia, High strength, nano-structured Mg-Al-Zn alloy, Mater. Sci. Eng. A 528 (2011) 2180-2191.
[29] M. Pozuelo, Y.W. Chang, J.M. Yang, Enhanced compressive strength of an extruded nanostructured Mg–10Al alloy, Mater. Sci. Eng. A 594 (2014) 203-211.
[30] D. Guan, W.M. Rainforth, J. Sharp, J. Gao, I. Todd, On the use of cryomilling and spark plasma sintering to achieve high strength in a magnesium alloy, J. Alloys Compd. 688, Part A (2016) 1141-1150.
[31] S.R. Kalidindi, A. Abusafieh, E. El-Danaf, Accurate characterization of machine compliance for simple compression testing, Exp. Mech. 37 (1997) 210-215.
[32] W.-b. Fang, W. Fang, H.-f. Sun, Preparation of high-strength Mg–3Al–Zn alloy with ultrafine-grained microstructure by powder metallurgy, Powder Technol. 212 (2011) 161-165.
[33] W.-b. Fang, W. Fang, H.-f. Sun, Preparation of bulk ultrafine-grained Mg-3Al-Zn alloys by consolidation of ball milling nanocrystalline powders, Transactions of Nonferrous Metals Society of China 21, Supplement 2 (2011) s247-s251.
[34] F.R.N. Nabarro, Stress-driven grain growth, Scr. Mater. 39 (1998) 1681-1683.
[35] A.J. Haslam, D. Moldovan, V. Yamakov, D. Wolf, S.R. Phillpot, H. Gleiter, Stress-enhanced grain growth in a nanocrystalline material by molecular-dynamics simulation, Acta Mater. 51 (2003) 2097-2112.
[36] J. Jiang, S. Ni, H. Yan, Q. Wu, M. Song, New orientations between β′2 phase and α matrix in a Mg-Zn-Mn alloy processed by high strain rate rolling, J. Alloys Compd. 750 (2018) 465-470.
[37] A. Singh, A.P. Tsai, Structural characteristics of β1′ precipitates in Mg–Zn-based alloys, Scr. Mater. 57 (2007) 941-944.
[38] D. Orlov, D. Pelliccia, X. Fang, L. Bourgeois, N. Kirby, A.Y. Nikulin, K. Ameyama, Y. Estrin, Particle evolution in Mg–Zn–Zr alloy processed by integrated extrusion and equal channel angular pressing: Evaluation by electron microscopy and synchrotron small-angle X-ray scattering, Acta Mater. 72 (2014) 110-124.
[39] X. Gao, J.F. Nie, Characterization of strengthening precipitate phases in a Mg–Zn alloy, Scr. Mater. 56 (2007) 645-648.
[40] C.C. Koch, D.G. Morris, K. Lu, A. Inoue, Ductility of nanostructured materials, MRS Bull. 24 (1999) 54-58.

Table 1 Summary of compressive properties of bulk CG, CM6h and CM6h+Eu samples

Samples	0.2% Proof Stress (MPa)	True Ultimate Strength (MPa)	True strain at ultimate strength
CG	187	363	0.130
CM6h	400	500	0.036
CM6h+Eu	408	506	0.066

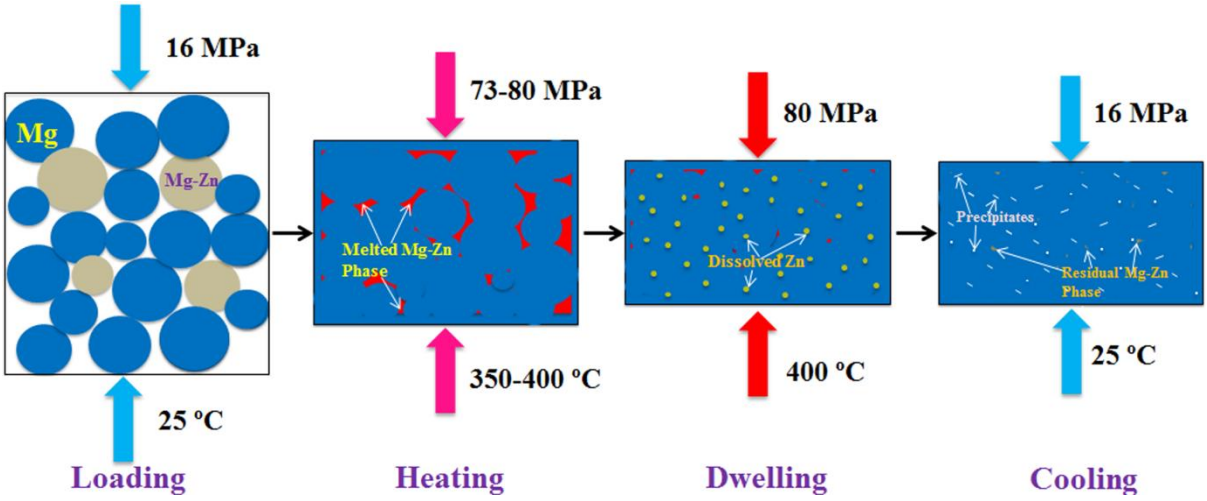

Fig. 1 Schematics showing the microstructural development due to *in-situ* powder casting during SPS process

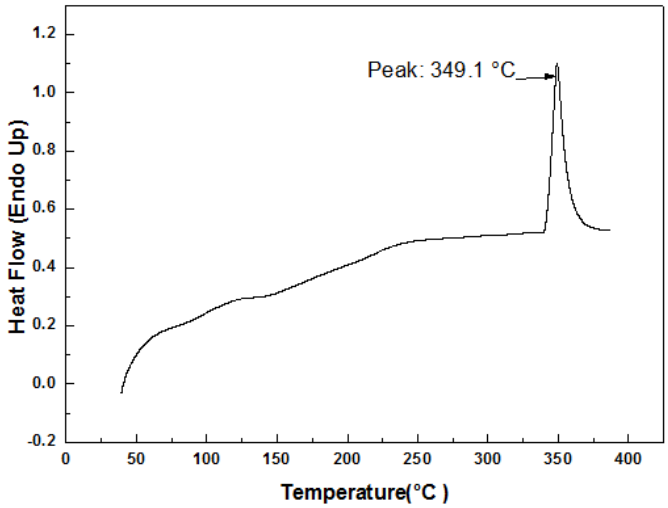

Fig. 2 A DTA curve showing the melting temperature of Mg-Zn eutectic alloy powder

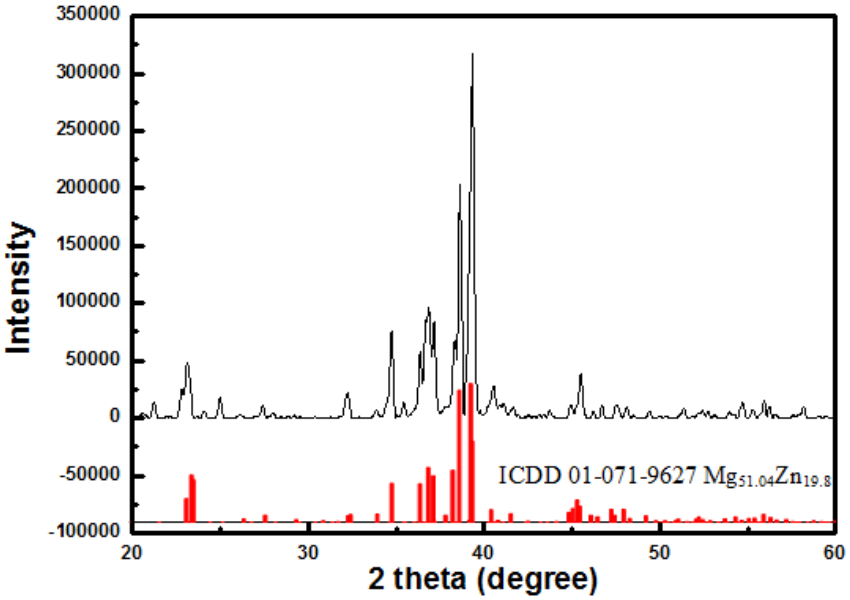

Fig. 3 XRD pattern of eutectic Mg-Zn alloy powder

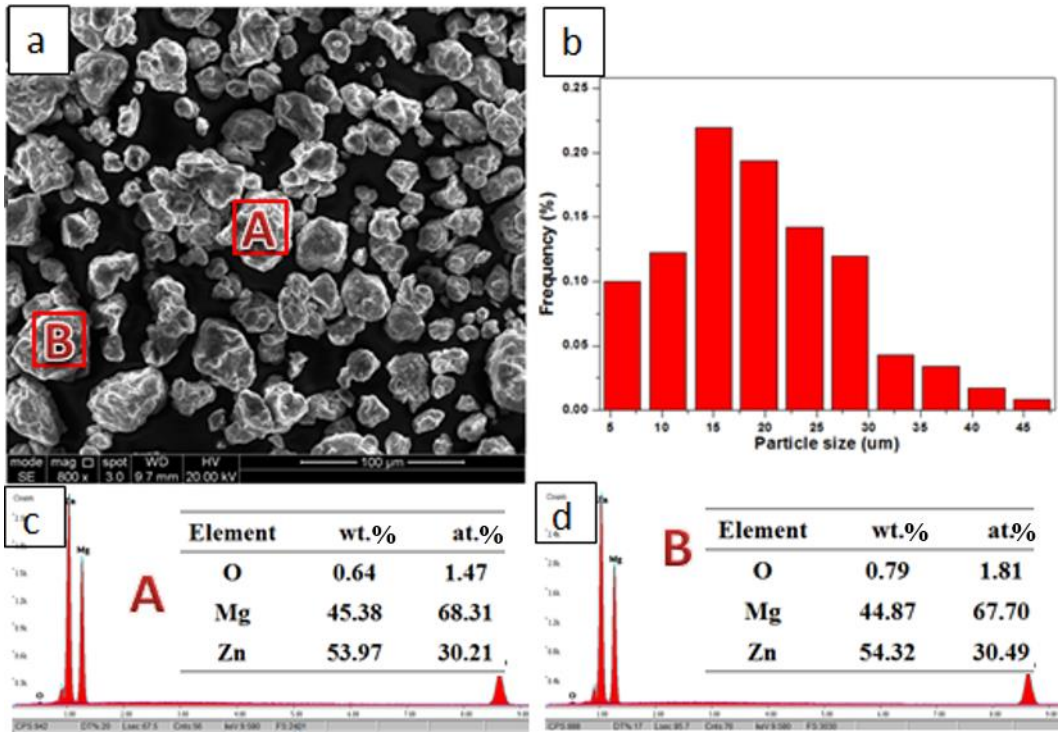

Fig. 4 (a) A representative secondary electron SEM image showing the morphology, (b) particle size distribution of Mg-Zn eutectic alloy powder, EDS spectra and quantitative values (inset) from the marked particles (c) A and (d) B

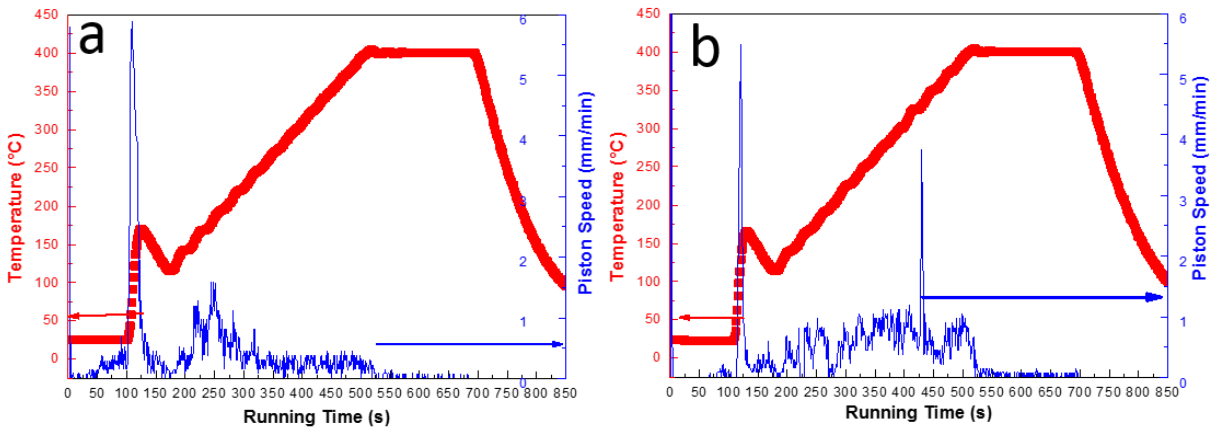

Fig. 5 The sintering temperature and piston speed as functions of time of bulk samples (a) CM6h and (b) CM6h+EA

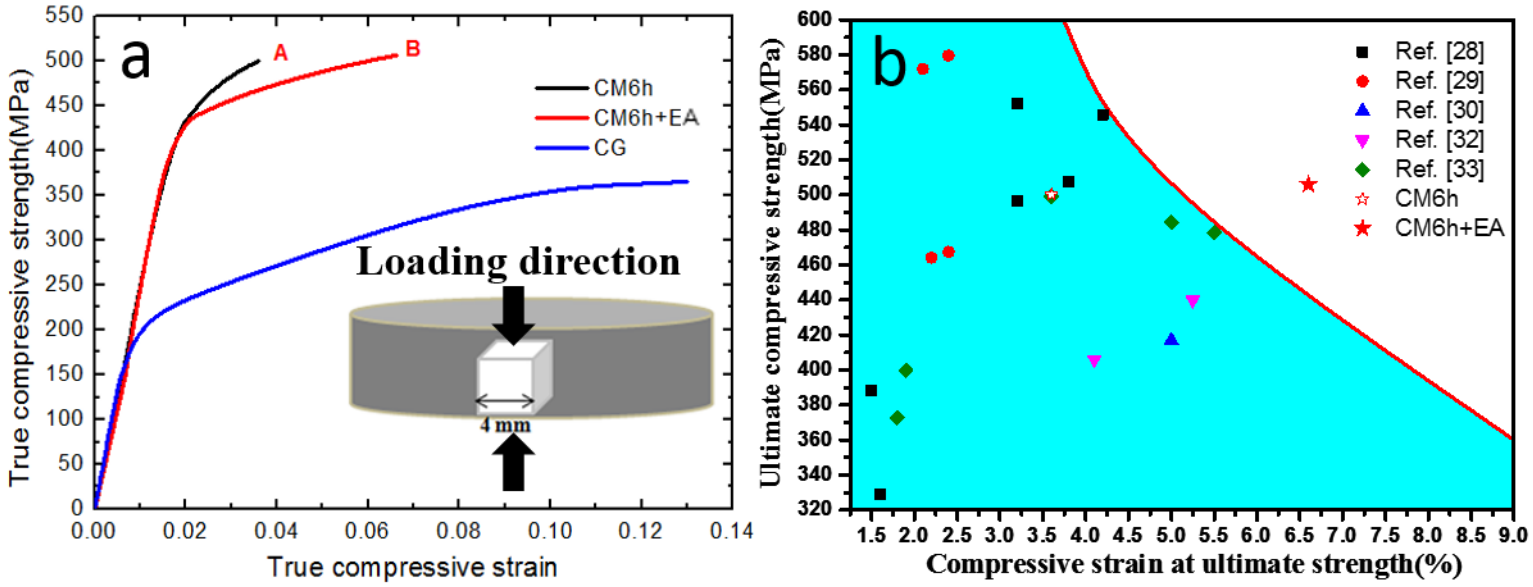

Fig. 6 (a) True compressive stress–strain curves of CM6h, CM6h+EA and CG samples, (b) ultimate strength versus strain of bulk NS Mg alloys

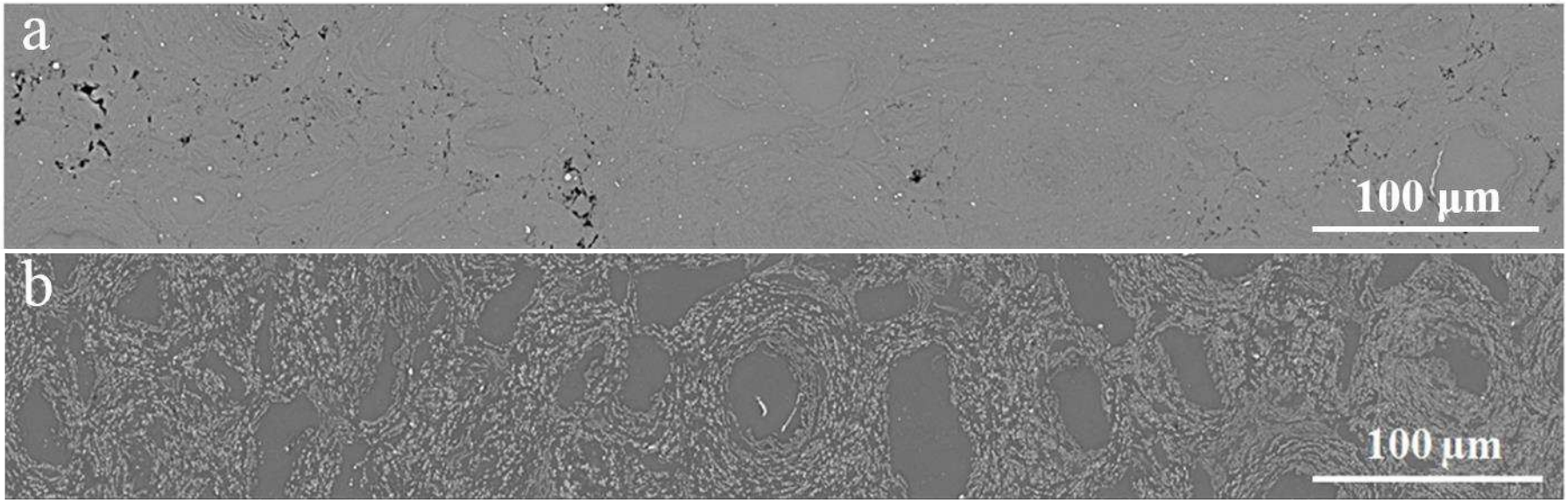

Fig. 7 Representative back scattered SEM images of samples (a) CM6h and (b) CM6h+EA

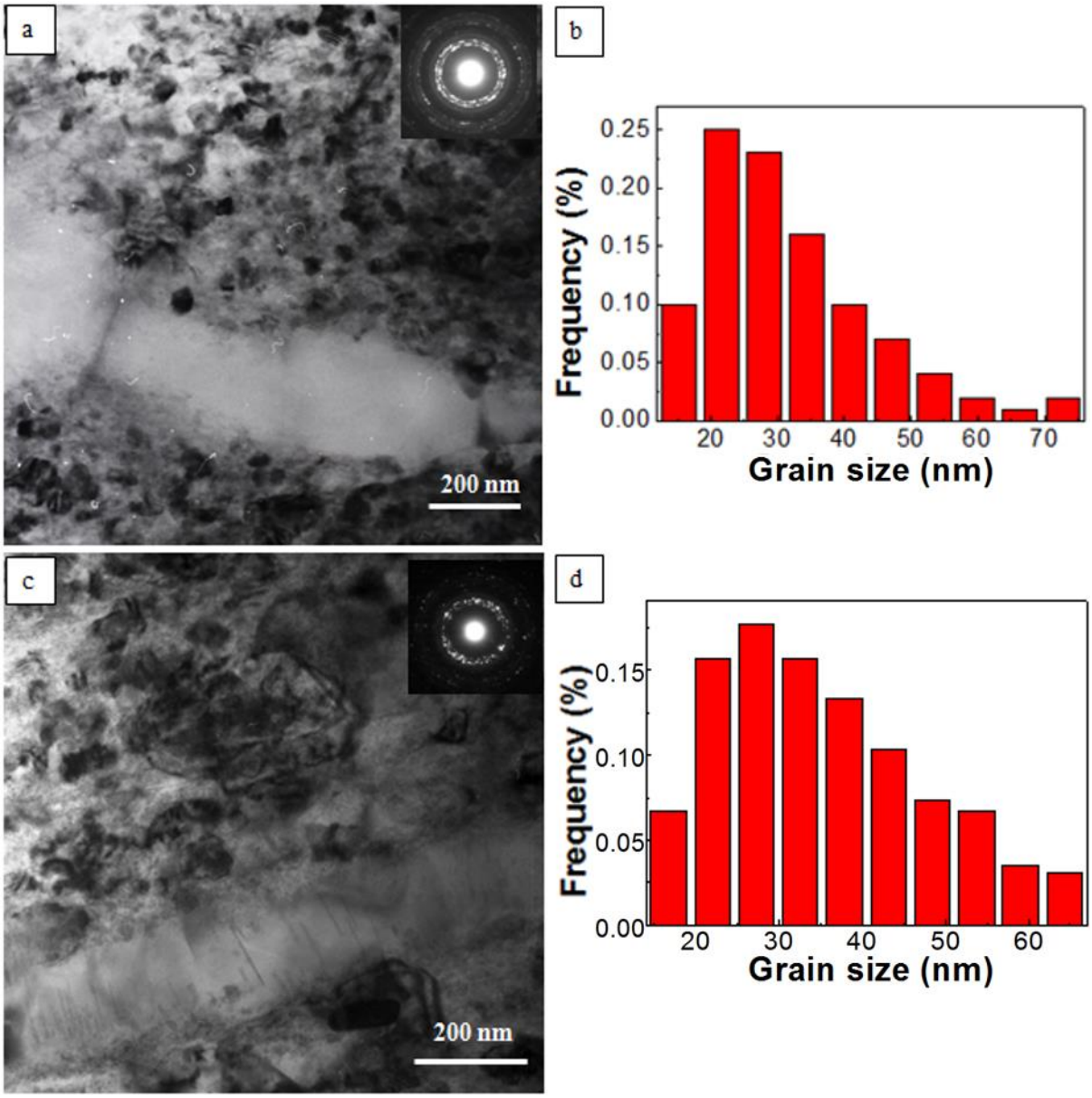

Fig.8 (a) A representative bright-field TEM image and SAED of sample CM6h, (b) corresponding statistical grain size distribution, (c) a representative bright-field TEM image and SADP of sample CM6h+EA and (d) corresponding statistical grain size distribution

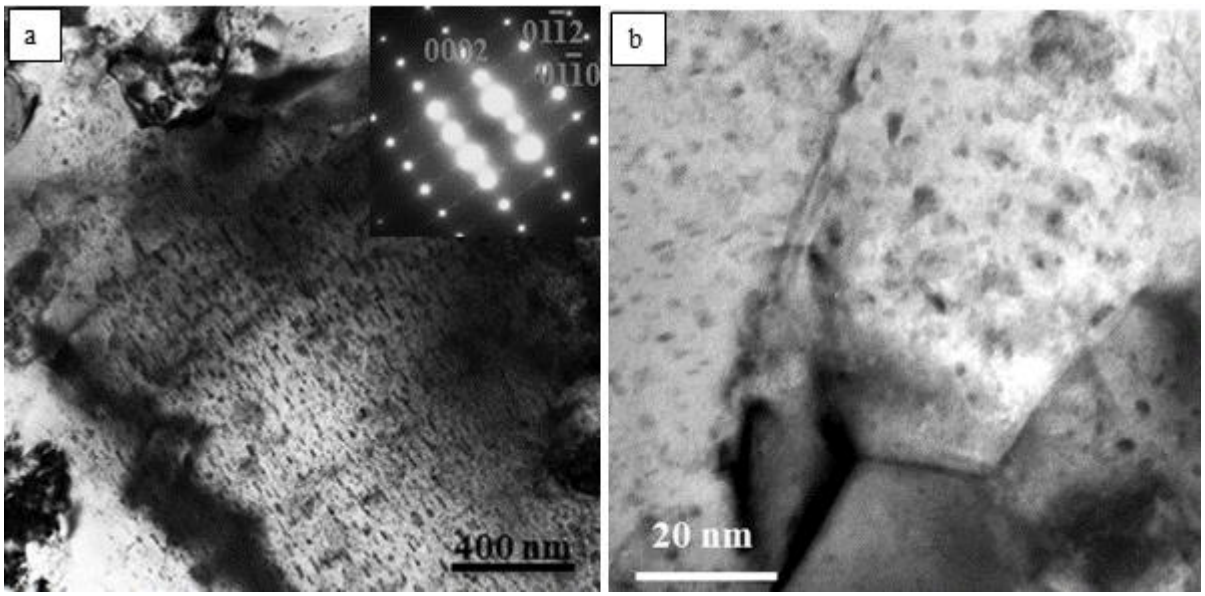

Fig. 9 TEM bright-field images and SADP of sample CM6h+EA (a) coarse grain (zone axis B//[2$\bar{1}$ $\bar{1}$0]) and (b) NC grains area